An Investigation into the Spectral Imaging of Hall Thruster Plumes

IEPC-2015-416／ISTS-2015-b-416

Presented at Joint Conference of 30th International Symposium on Space Technology and Science,
34th International Electric Propulsion Conference and 6th Nano-satellite Symposium
Hyogo-Kobe, Japan
July 4–10, 2015

Michael R. Nakles*
ERC, Inc., Edwards Air Force Base, CA, 93524

Michael R. Holmes† and William A. Hargus, Jr.‡
Air Force Research Laboratory, Edwards Air Force Base, CA, 93524

An exploratory investigation of measuring xenon spectral emission lines in a Hall thruster plume through optical imaging techniques was performed on the SPT-100 Hall thruster. A 16 bit CCD camera was used with optical interference bandwidth filters to separately photograph neutral (823 nm) and singly charged ion (542 nm) xenon emission. The resulting images allowed for examination of the near-plume structure in terms of excited ions and neutral particles for various thruster operating conditions. Abel inversion analysis was applied to the photographs to examine the emission as a function of radius with the assumption of axial symmetry and an optically thin plasma. This experimental technique may provide results useful for comparison with numerical near-plume predictions that incorporate collisional radiative models.

Nomenclature

A_{lens} area of lens aperture
A_n amplitude coefficients for the cosine series expansion fit in the Fourier Abel inversion method
A_{pixel} area of a CCD pixel
A_R Abel inversion of radiance
c speed of light in vacuum
C constant that accounts for optical geometry parameters and physical constants in optical calibrations
I_d anode discharge current
$f(r)$ radially dependent function
$f_n(r)$ set of cosine functions in the Fourier Abel inversion method
$F(Y)$ line-of-sight integration of $f(r)$ along x-axis
f_λ fractional transmittance of neutral density filter at wavelength λ
h Planck's constant
$\dot{m}_a$ anode propellant mass flow rate
$\dot{m}_b$ mass flow rate of additional background gas
$\dot{m}_c$ cathode propellant mass flow rate
n CCD count value
N_l lower frequency limit for the cosine series expansion in the Fourier Abel inversion method
N_u upper frequency limit for the cosine series expansion in the Fourier Abel inversion method
P vacuum chamber pressure

*Research Engineer, ERC, Inc., 1 Ara Rd. Edwards AFB, CA 93524
†Research Scientist, AFRL/RQRS, 1 Ara Rd. Edwards AFB, CA 93524
‡Research Engineer, AFRL/RQRS, 1 Ara Rd. Edwards AFB, CA 93524

Q_λ	quantum efficiency of CCD at wavelength λ
r	radial coordinate about thrust axis (z-axis)
R	radiance or maximum value of radius in the domain of the cylindrically symmetric function
s'	distance between lens and CCD
V_d	anode discharge voltage
x	axis in thruster coordinate system perpendicular to the cathode plane (see Fig. 4)
y	axis in thruster coordinate system in the cathode plane (see Fig. 4)
z	axis in thruster coordinate system in thrust direction (see Fig. 4)
Δt	image exposure time
λ	wavelength

Introduction

Hall effect thruster plumes present a challenging environment for the implementation plasma diagnostics. The near-plume region is an especially difficult region to characterize where changes in density and temperature occur over short distances. Here, the physical presence of probes is likely to perturb the plasma, affect thruster operation, cause heating effects, and lead to physical degradation of the probe itself. Even sizing a probe small enough for good spatial resolution can be difficult. Optical diagnostics such as laser-induced fluorescence[1] and microwave interferometry[2] are not encumbered by these limitations and have proven useful for reliable near-plume measurements.

The idea of using photography for certain types of plasma characterization is intriguing for its potential advantages. Images provide data in a virtually continuous fashion over a wide measurement domain, whereas most other diagnostics typically measure at one physical location at a time and must be physically moved to create a set of discrete data. The location of the camera outside of the vacuum chamber avoids physical disruption of the plasma and allows convenient access for the operator. Photographic images have been used to visually inspect basic changes in plume structure for different thruster operating modes.[3,4] Modern high-speed cameras can record images on timescales that allow the study of plasma oscillation modes in discharge channels.[3,5] Photography with optical filters has been used to image xenon ion and neutral emission separately in an ATON A53 Hall thruster.[6] This data was transformed from line-of-sight data into cross-sectional images of the plume for two operational modes through an inverse Abel transformation.

In this study, a 16 bit camera with optical interference bandwidth filters was used to examine the plasma structure of the near-plume of the SPT-100 in terms of optical emission of the 542 nm xenon ion line and the 823 nm xenon neutral line for various operating conditions. Optical emission is a function of both plasma density and temperature and can be predicted by collisional radiative models. The goal of this study was to examine the structure of the near-plume of the SPT-100 thruster at various operating conditions and to explore the use of Abel inversion analysis to deconvolve the image line-of-sight data into a radially dependent function with the assumption of axial symmetry and an optically thin plasma. The results of this experimental imaging may provide a useful comparison tool for numerical simulations of the near-plume region that incorporate collisional radiative models.

Experimental Apparatus and Techniques

Hall Effect Thruster

A flight model SPT-100 Hall effect thruster (Fig. 1) was used in this study. The axisymmetric thruster is equipped with two lanthanum hexaboride (LaB_6) cathodes (only one was used during these tests). This thruster has a conventional five core (one inner, four outer) magnetic circuit. Discharge current is routed through the magnetic circuit and thus no extra power supply for the magnets is required. The acceleration channel of the thruster has a 100 mm outer diameter, a 69 mm inner diameter, and a channel depth of 25 mm. For its nominal xenon operating condition, the thruster has been characterized to have a thrust of 83 mN with a specific impulse of 1,600 s, yielding an anode efficiency near 50%.[7]

For this study, the thruster and cathode were powered with commercial off-the-shelf Sorenson power supplies instead of the PPU used on-orbit. A computer data acquisition system recorded the potential and current outputs of the power supplies used in the thruster operation at a rate of 2 Hz. For propellant flow, digital mass flow controllers from Aera dispersed gas to the anode and cathode taking the place of the xenon flow control system (XFC) used on-orbit. Therefore, propellant flow rate was constant for each given operating condition and not controlled by discharge current feedback as with an XFC system.

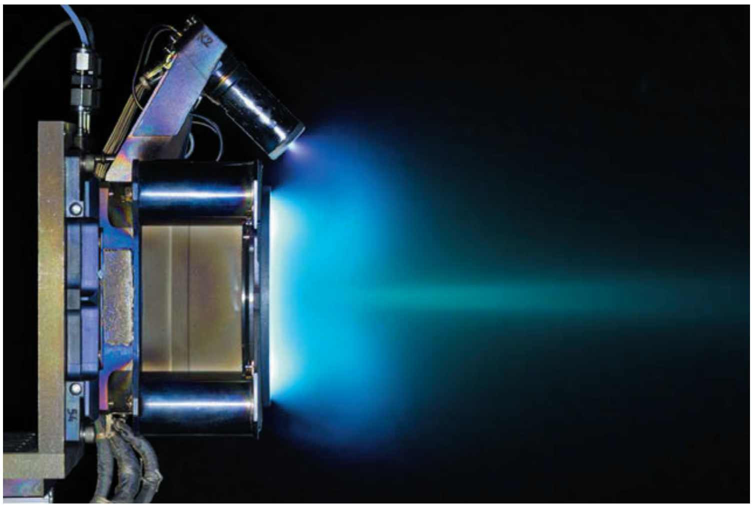

Figure 1. The SPT-100 firing in Chamber 1 photographed by a digital SLR from the same perspective as the scientific images presented in this study.

Test Facility

This study utilized Chamber 1 (Fig. 2(a)) at the Air Force Research Laboratory at Edwards Air Force Base. Chamber 1 is a cylindrical non-magnetic stainless steel vacuum chamber 2.4 m in diameter and 4.1 m in length. Pumping is provided by two liquid nitrogen baffled (70 K), 1.2 m flanged gaseous helium two stage cryogenic (15 K) vacuum pumps with a measured pumping speed on xenon of 48,500 L/s. Chamber pressure is monitored with a hot filament ionization gauge.

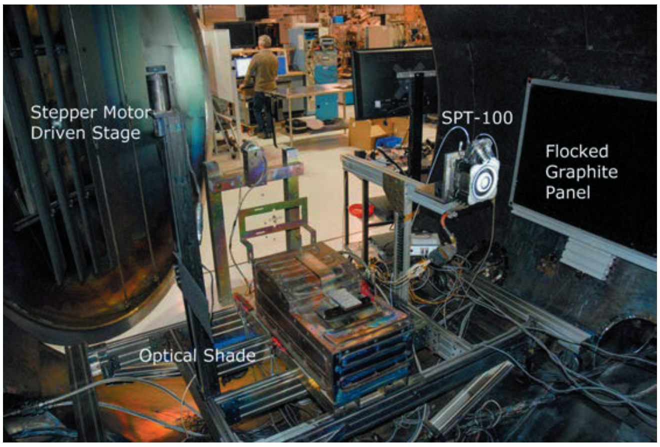

(a) The SPT-100 installed in Chamber 1. The optical viewport for imaging is beyond the left photo border.

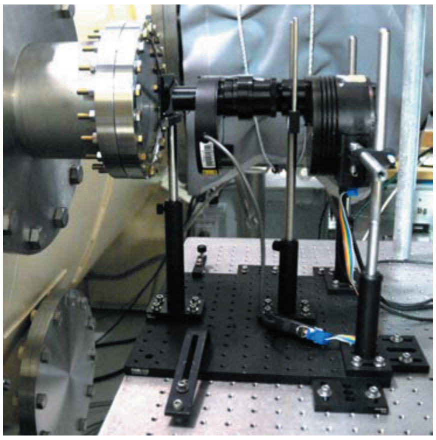

(b) The SBIG ST-10XE camera and optical components.

Figure 2. Experimental Setup

Optical Components

Camera

A Santa Barbara Instruments Group (SBIG) ST-10XE 16 bit CCD camera (Fig. 2(b))was used for this imaging experiment. It employs a Kodak KAF-3200E 3 megapixel CCD (2184×1472 with 6.8 μm pixels). The camera was designed for astronomical imaging and thus long exposure durations (the fastest shutter speed is 0.12 s). It interfaces with t-mount optical components. The instrument has an electronic chiller to reduce thermal image noise, which was set to 5°C for these measurements. A 70 mm focal length lens was mounted to the camera along with a variable aperture diaphragm set to a 9.7 mm diameter making for an f-number of f/7.2. Optical filters were stored and positioned with an SBIG CW-8 electronic filter wheel. The camera was controlled with a laptop PC. See Fig. 4 for a schematic of the optical set up.

Filters

Two 25 mm diameter interference filters from Custom Scientific were used to isolate xenon spectral emission lines. Singly charged ion emission was photographed through a bandwidth filter centered at 542 nm filter with a transmission distribution function having a full width at half maximum (FWHM) of 10 nm. Neutral xenon emission was photographed with a filter centered at 823 nm also with a FWHM of 10 nm. Besides collecting signal from the 823 nm neutral line, this filter also gathers emission from the 828 nm neutral line. The high f-number of the optical setup prevented light with high incidence angle from reaching the CCD, which minimized potential filter tuning effects. Figure 3 shows the filter transmission functions (blue traces on plot insets) along with the spectral radiance of the SPT-100 measured with a spectrometer through a diffuse optical collector.

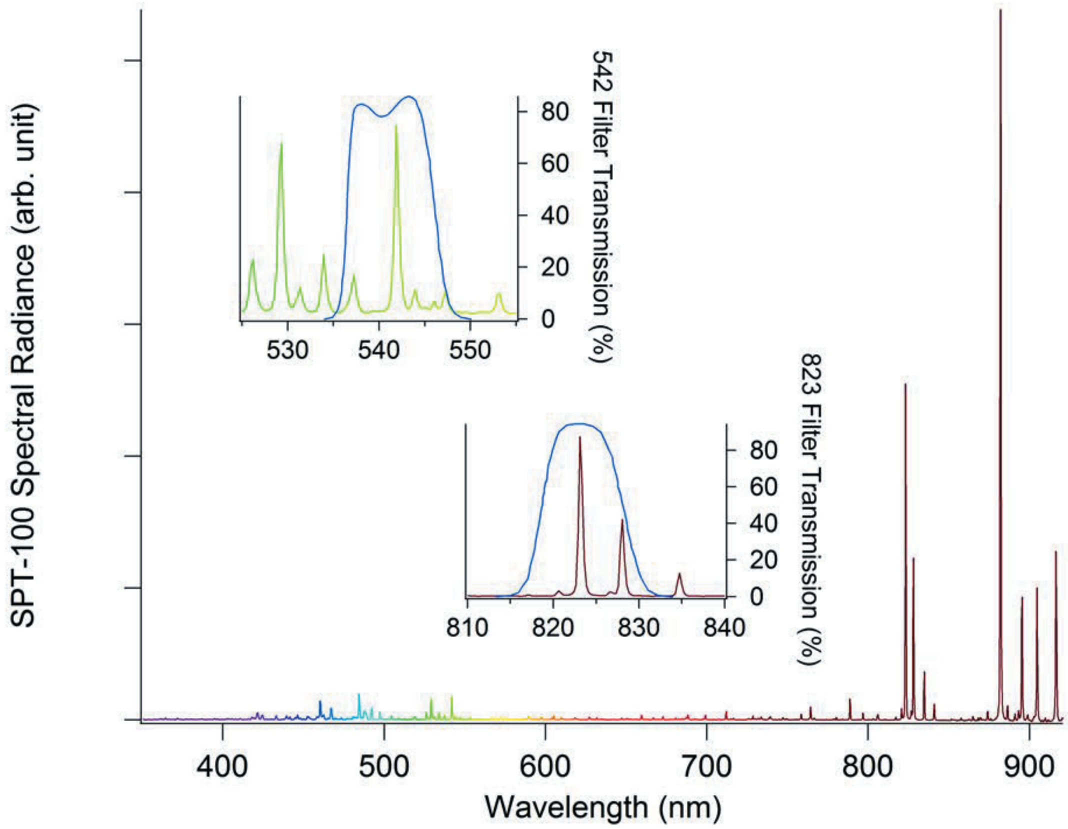

Figure 3. Spectral radiance of the SPT-100 plume measured with a spectrometer and optical interference filter transmission curves (blue traces on plot insets).

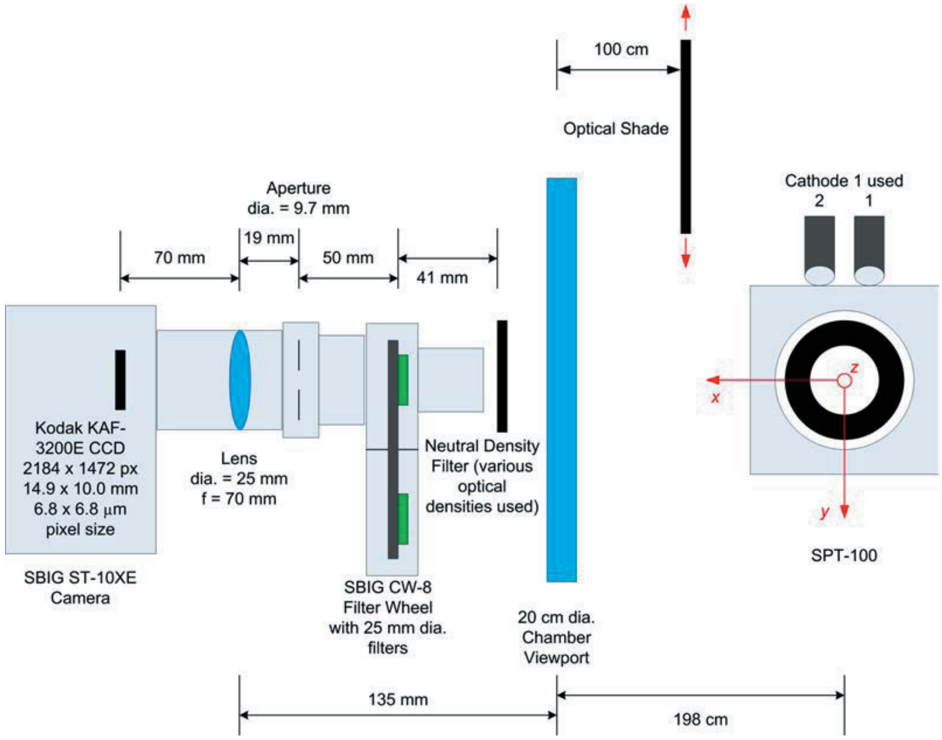

Figure 4. Schematic of optical setup and thruster coordinate system.

Testing Methodology

Optical Techniques

The SPT-100 was mounted with its centerline 198 cm from a 20 cm dia. optical view port on a lateral side of the vacuum chamber. The camera was mounted on an optics table outside the chamber and pointed through the window for a profile view of the thruster and plume (Figs. 1 and 4). A flocked graphite panel was placed on the chamber wall opposite of the window to serve as an non-reflective black background for the images.

The shiny surfaces of the optical interference filters in conjunction with the other optical surfaces created a mirrored and inverted reflection of the plume about the vertical centerline of the photo that appeared in the camera images. Constraining the plume image to one side of the frame was necessary to prevent unwanted reflections from becoming superimposed on the primary plume image. Thus, the thruster was framed in the camera's field of view with its plume confined to the right half of the frame (with its downstream axis pointing rightward). Unfortunately, this solution to the reflection problem required discarding one half of the image area.

A motion stage controlled optical shade (Figs. 2(a) and 4) was constructed from a grafoil (flexible graphite) sheet covered with graphite felt and placed inside the chamber so that certain regions of the thruster, which varied drastically in brightness, could be selectively blocked from the view of the camera. The shade could be positioned so that it blocked the cathode (very bright neutral emission) or the region of the plume upstream of $z = 134$ mm. Blocking bright regions of emission allowed for exposures of dimmer regions that more fully utilized the bit depth of the CCD by preventing overexposed regions with pixel bleeding. In some cases, separate exposures for different regions were combined to form a composite photo, effectively increasing the dynamic range of the image. Three different neutral density filters (powers of 0.75, 2.0, and 2.5) were used to enable exposure times of between 1 s and 30 s and were selected based on the brightness of the region being photographed.

To improve the signal to noise ratio in the photographs, 10 exposures were averaged for each image. A dark frame (photo with shutter closed) for the same exposure duration and same CCD temperature was subtracted to remove noise caused by thermal effects. Images were also corrected with flat field images, which are images of a uniformly illuminated flat surface. Images are divided by the flat field image to correct for vignetting and variations in pixel response. Flat field corrections are important in photometric studies such as the present one where vignetting caused up to a 60% brightness variation between the image center and corner in uncorrected images.

Calibrations of the optical system were performed by photographing an integrating sphere inside the chamber illuminated by an Oriel Model 63355 quartz tungsten halogen lamp with a NIST traceable irradiance curve. Calibration photographs were used to determine the fractional transmittance of each neutral density filter at 542 nm and 823 nm. The relative quantum efficiency of the CCD at 542 nm and 823 nm was also measured through calibration photos. With knowledge of these parameters, images taken with different neutral density filters and interference filters could be scaled relative to each other in terms of radiance according to Eq. 1.

$$R = \frac{n}{f_\lambda Q_\lambda \frac{\lambda}{hc} A_{pixel} \frac{A_{lens}}{s'^2} \Delta t} = \frac{Cn}{Q_\lambda \lambda \Delta t f_\lambda} \tag{1}$$

so that

$$\frac{R_1}{R_2} = \frac{n_1}{n_2} \frac{Q_{\lambda 2}}{Q_{\lambda 1}} \frac{\lambda_2}{\lambda_1} \frac{\Delta t_2}{\Delta t_1} \frac{f_{\lambda 2}}{f_{\lambda 1}} \tag{2}$$

Tests were performed to measure pixel response with exposure time to determine the point near the upper limit of pixel count range where the CCD response became nonlinear. All image exposure times were selected to ensure that pixel counts never exceeded the linear response limit (Fig. 5).

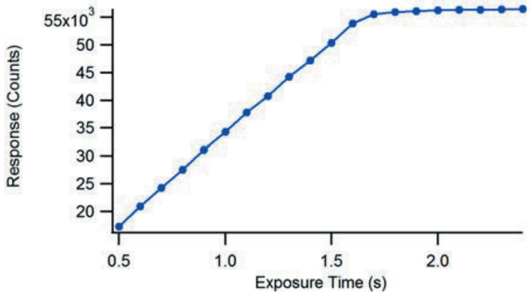

Figure 5. Linearity in CCD response was maintained for count values of less than 50,000.

Inverse Abel Transformation

The photographic images in this study can be considered to approximate a line-of-sight data set where plume emission is integrated along the x-axis of the thruster coordinate system (see Fig. 4). In order to study emission as a function of r, an Abel inversion was applied to image data. Besides the line-of-sight assumption, the plasma was also assumed to be optically thin and axially symmetric about the z-axis for a given direction of the y-axis. In this study, the half of the plume in the positive y-axis (non-cathode side) was chosen for Abel analysis because it was assumed to have a higher degree of symmetry due to less perturbation from cathode.

The forward Abel transform for a radially symmetric function, $f(r)$ is given by[8]

$$F(y) = 2 \int_y^\infty \frac{f(r) r dr}{\sqrt{r^2 - y^2}} \tag{3}$$

and the analytical inverse transformation is

$$f(r) = -\frac{1}{\pi} \int_r^\infty \frac{dF}{dy} \frac{dy}{\sqrt{y^2 - r^2}} \tag{4}$$

The inverse Abel transform is impractical to solve directly through numerical means due to the fact that it requires differentiation of experimental data, which may be noisy, and contains a singularity.[9] Inverse problems by nature are unstable and tend to amplify noise. There are many types of approaches to performing the inverse Abel transform.[9–12]

Two Abel inversion techniques were tested on the data from this study. The first was an "onion-peeling" method with Tikhonov regularization as described in Ref. 12. The "onion-peeling" method works by discretizing Eq. 3 and assuming that $f(r)$ is a constant value for each of a series of concentric rings about the axis of symmetry. A system of linear equations based on geometry is solved through a least squares method to determine $f(r)$. Tikhonov regularization with a first-order operator was used as a smoothing constraint in the least squares calculation. A disadvantage of the "onion-peeling" method is that the error in the outer regions of the domain propagate inward making the center region the most uncertain.[10]

An Abel inversion method that avoids this problem is the Fourier Method described in Ref. 10 where the unknown function $f(r)$ is constructed from a series expansion of cosine terms each multiplied by an amplitude factor. So that

$$f(r) = \sum_{n=N_l}^{N_u} A_n f_n \tag{5}$$

where

$$\begin{aligned} f_0(r) &= 1 \\ f_n(r) &= 1 - (-1)^n \cos\left(n\pi \frac{r}{R}\right) \end{aligned} \tag{6}$$

The amplitude value for each cosine term is determined through a least squares fit of the forward Abel transform equation (Eq. 3) with the line-of-sight data. The lower and upper limit for the number of cosine terms can be adjusted to optimize the fit for the expected distribution shape and the upper limit also acts as a low-pass filter for noise in the measured data. In the present analysis, a lower frequency of 0 and upper frequency of 50 was used in the inversions.

Thruster Operating Conditions

Thruster operating conditions for imaging were selected so that the effects of background pressure, discharge voltage, and propellant flow rate on emission could be characterized. The operating conditions photographed are summarized in Table 1. To artificially increase chamber background pressure, extra xenon gas was flowed into the chamber through a feed-through at the chamber wall that was 5 cm downstream from the thruster exit plane and 70 cm from the thruster center line. Discharge voltage and propellant flow rate values were increased and decreased by 30% of their nominal values. It is important to note that varying propellant flow rate also affects this thruster's magnetic field because the discharge current is routed through the magnet coils. Therefore, changes in the plume emission for these cases are a result of both factors.

Operating Condition	V_d **(V)**	I_d **(A)**	**Power (W)**	$\dot{m}_a$ **(mg/s)**	$\dot{m}_c$ **(mg/s)**	$\dot{m}_b$ **(mg/s)**	P **(Torr-Xe)**
Nominal	300	4.61	1383	5.15	0.40	0.00	2.28E-05
High Back. Press.	300	4.57	1371	5.15	0.40	4.22	4.55E-05
Low Dis. Voltage	210	4.60	966	5.15	0.40	0.00	2.09E-05
High Dis. Voltage	390	4.56	1778	5.15	0.40	0.00	2.08E-05
Low Prop. Flow Rate	300	2.90	870	3.60	0.28	0.00	1.52E-05
High Prop. Flow Rate	300	5.99	1797	6.69	0.51	0.00	2.74E-05

Table 1. Thruster operating specifications.

Results

Overview

For each parameter variation, radiance photograph sets are presented for 542 nm and 823 nm emission showing the low and high value parameter cases side-by-side along with an image showing the change in radiance of the high value parameter case relative to the low value case (Figs. 6, 7, 11, 12, 15, and 16). For the delta images, gaussian smoothing was applied to the original images to control noise amplified through division. A consistent (except for the high propellant flow rate cases) linear color scale, which reveals features in the first 100 mm downstream of the exit plane, was applied to the images to facilitate comparison of the various operating conditions. Note that some of the highest intensity regions of the plume near the exit plane exceeded the maximum range of the color scale and are colored dark gray. Radiance decays rapidly beyond about one thruster diameter downstream of the exit plane. Therefore, logarithmic contour lines were used to delineate the shape and magnitude of the radiance. The lowest value contour lines were sometimes omitted where the data was exceptionally noisy. Blocks were added to the images to denote the channel geometry.

Abel inversion analysis was performed on these images to examine cross-sections of emission. Both the "onion-peeling" and Fourier inversion methods produced good results that matched well. The Fourier method was observed to preserve slightly better detail in the central region of the plume that revealed the subtle dove-tail feature of the ion jet while producing an adequately smooth solution with low noise in the low-intensity regions of the plume. Thus, the Fourier method was chosen as the Abel inversion technique for the present data set. These results and their corresponding delta images are shown in Figs. 8, 13, and 17. In certain areas near the plume centerline, the inversion produced negative values. These negative value regions were calculated by both inversion techniques and were assumed to be caused by asymmetry in the plume. For the background pressure and discharge voltage variation cases, radial profiles of the Abel inversion are shown at six different z-axis locations (2.5, 5, 10, 20, 40, and 80 mm) and are presented along with the corresponding line-of-sight radiance data (Figs. 9 and 14).

Background Pressure Variation

Figures 6 and 7 show the 542 and 823 nm emission photographs, respectively, for the background pressure variation. These photos show a distinct change of emission structure of the plume for high background pressure where both ion and neutral emission decrease in the plume central core beyond $z = 50$ mm and increase in the laterally surrounding areas. With the exception of the plume core, 823 nm emission increases throughout the measurement domain due to the higher density of neutral xenon atoms. However, Fig. 6(c) shows a 10% decrease in 542 nm emission immediately downstream of the center magnetic pole within 20 mm of the exit plane while emission directly downstream of the acceleration channel remains nearly constant.

The region of decreased emission in the center of the plume may indicate a decrease of interaction between ion beams from opposite sides of the acceleration channel due to a smaller beamlet divergence angle at the exit plane. A study of the effects of background pressure on the SPT-100 performance observed that thrust increases with increasing background pressure.[13] This thrust increase was attributed mostly to decreased plume divergence as measured by probes, which may have been caused by the ion acceleration zone shifting to a more upstream location in the discharge channel likely due to increased electron mobility from Bohm diffusion due to the higher rate of electron-neutral collisions. This upstream shift in the acceleration region with increased background pressure was also observed in Ref. 14 for the BHT-600 thruster.

Increased electron mobility may also be the reason that the plume emission appears to become more symmetric for high background pressure so that the cathode and non-cathode sides of the image are more similar as emission increases significantly in the region opposite of the cathode about the y-axis. This effect is observed in the delta images that show highly increased 823 nm emission (and 542 nm emission to a lesser degree) near the exit plane outside of the acceleration channel near $y = 75$ mm.

Abel inversion of ion emission in Figs. 8(a), 8(c), and 9(a) shows a Gaussian shaped distribution emanating from the discharge channel for both background pressures. Fig. 8(c) shows close similarity through $z = 20$ mm. At 40 mm and beyond, the lower emission at center of the plume is consistent with the observations made from the line-of-sight data.

Neutral emission cross sections (Figs. 8(b), 8(d), and 9(b)) show a distinctly different radial profile near the exit plane than the ion emission with maxima at the edges of the acceleration channel and a dip in the center. Interestingly, this distribution profile along the channel exit is consistent with laser-induced fluorescence measurements of neutral density for the SPT-140 described in Ref. 15. Unlike the ion radial profiles, the neutral profiles change quickly between the two pressure cases with downstream distance. At $z = 10$ mm the local maxima from the discharge channel edges disappears for the high pressure case (Fig. 8(e)) and the lobe shaped region of emission centered at $y = 75$ mm and $z = 30$ mm becomes more prominent as shown in Fig. 7(c).

Ion/Neutral Emission Comparison for Nominal Case

The difference between 542 and 823 nm emission for the nominal operating condition is presented in Fig. 10. Throughout the plume, the radiance of the neutral line is stronger. The regions with the highest relative 542/823 emission are the central core of the plume beyond $z = 50$ mm and near the exit of the acceleration channel. The regions with the lowest relative emission are found in the lateral areas outside of the thruster plume where there are few ions.

Discharge Voltage Variation

Figures 11 and 12 show the emission for the discharge voltage variation operating conditions. Figure 11(c) shows that increasing discharge voltage increases ion emission in the plume core 100 mm downstream of the exit plane while it decreases elsewhere. This plume shape may be indicative of the higher energy ions undergoing collisions from geometrical beam interactions farther downstream. A similar, but broader collision region is seen for the neutral emission in Fig. 12(c) beyond $z = 50$ mm which may be from the beam ions colliding with the diffuse neutral propellant.

The ion emission profiles from Abel inversion shown in Fig. 9(a) show a similar shape between the two discharge voltage cases with the low discharge voltage case emission significantly stronger near the exit plane, but becoming nearly the same at $z = 80$ mm. The location of the peak ion emission for the low discharge voltage case is offset inward from the channel center by 1.1 mm at $z = 2.5$ mm and migrates inward with downstream distance so that it is 4.4 mm offset from channel center at $z = 20$ mm. In contrast, the high discharge voltage case emission peak stays closer to channel center with downstream distance so that it is only 0.9 mm offset at at $z = 20$ mm suggesting less divergent ion flow from the channel. This effect is also noticeable in the cross section data shown in Fig. 13.

The neutral emission profiles shown in Fig. 9(b) also shows a similar shape between the high and low discharge voltage cases where the low discharge case has higher emission within 20 mm of the exit plane. The profiles at $z = 40$ and 80 mm and Fig. 13(f) show a significant emission increase in the central plume.

Propellant Flow Rate Variation

Propellant flow rate effects (in combination with magnetic field effects) are shown in Figs. 15 and 16. Figures 15(b) and 16(b) show that at high propellant flow rate, the magnitude of the radiance becomes much greater and the plume emission appears spherical, likely due to a higher rate of scattering collisions with the higher density of un-ionized propellant. This emission shape is a drastic change from the other test conditions where the shape appears to be influenced by geometrical beam interactions. The Abel inversion cross sections shown in Fig. 17 also show the spherical emission shape. Figures 17(e) and 17(f) show a dramatic increase in emission just downstream of the center of the inner magnetic pole (especially for ion emission) and a region with little change in the plume central core beyond $z = 70$ mm for ion emission and $z = 120$ for neutral emission.

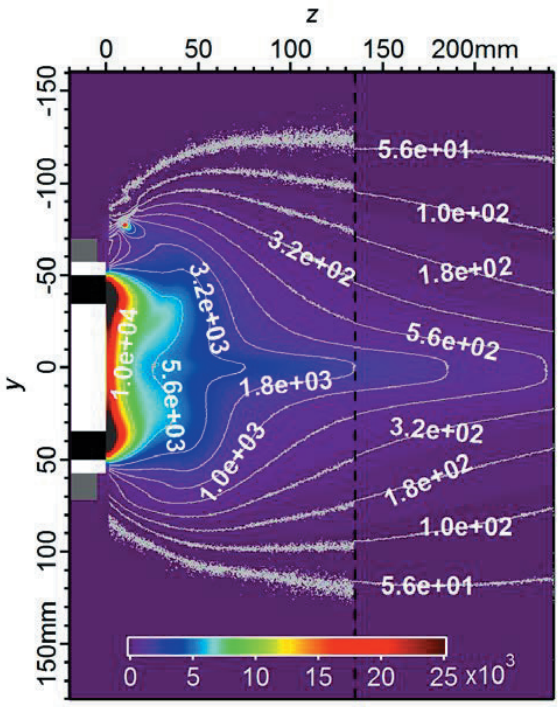

(a) Nominal Condition: 542 nm radiance (arb. unit)

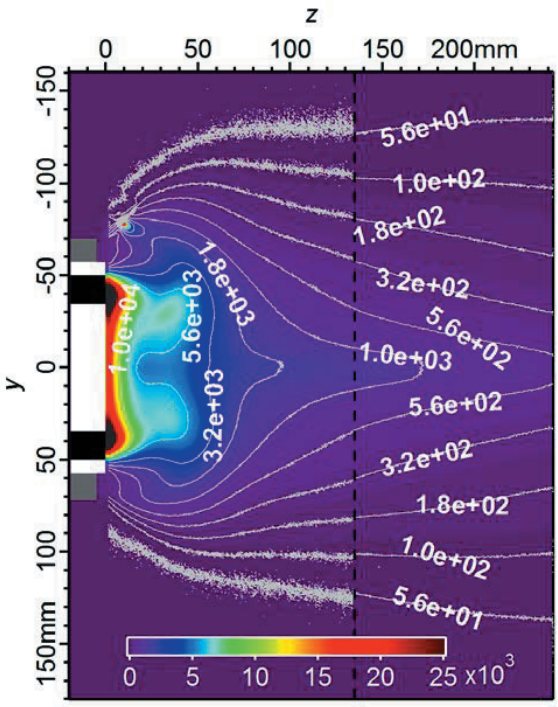

(b) Double Background Pressure Condition: 542 nm radiance (arb. unit)

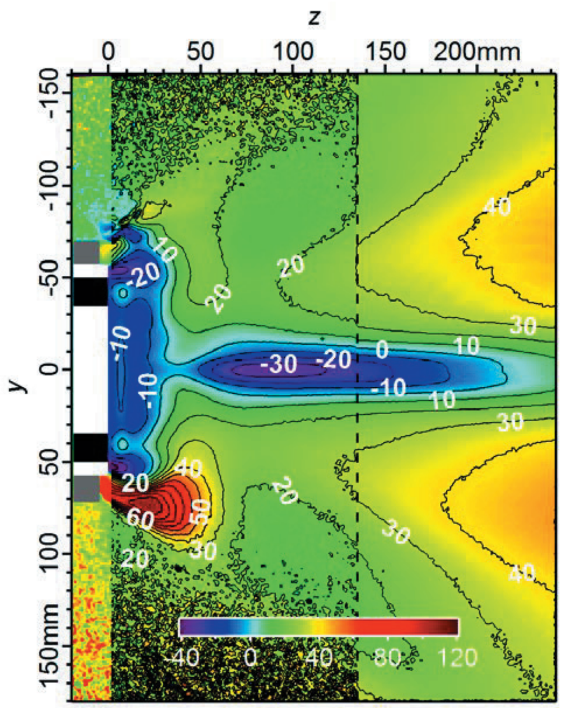

(c) Δ Radiance (%): $\frac{R_{542:DP} - R_{542:Nom}}{R_{542:Nom}} \times 100$

Figure 6. Ion emission radiance (542 nm) of the nominal operating condition and the double background pressure condition. Dark gray color in plume represents values greater than the color scale upper limit. Dotted lines mark boundaries of composite photos.

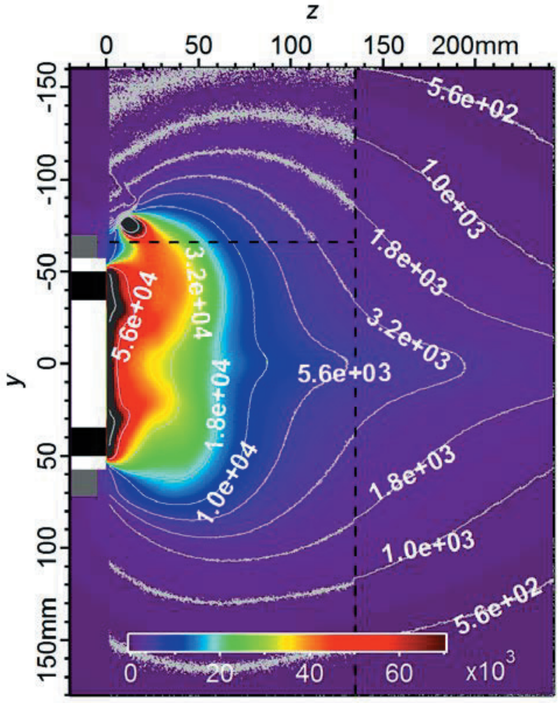

(a) Nominal Conditions: 823 nm radiance (arb. unit)

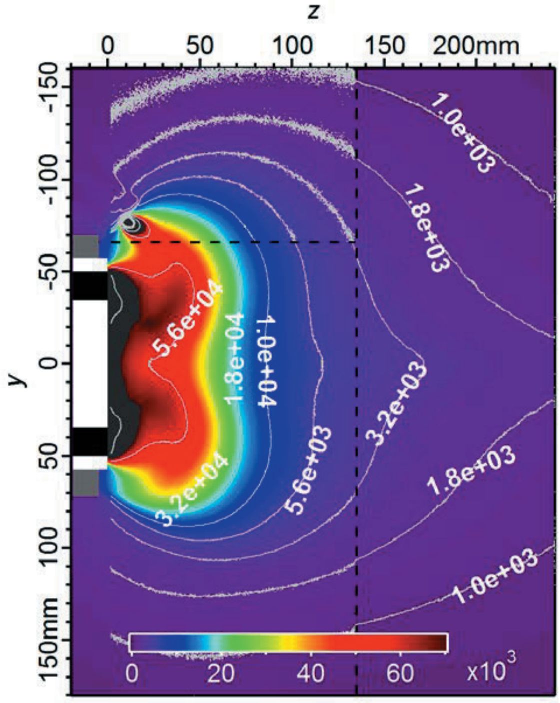

(b) Double Background Pressure Condition: 823 nm radiance (arb. unit)

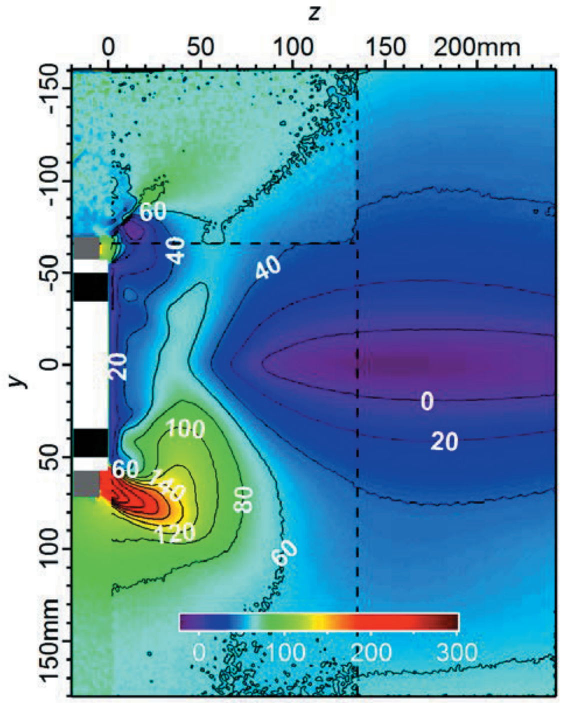

(c) Δ Radiance (%): $\frac{R_{823:DP} - R_{823:Nom}}{R_{823:Nom}} \times 100$

Figure 7. Neutral emission radiance (823 nm) of the nominal operating condition and double background pressure condition. Dark gray color in plume represents values greater than the color scale upper limit. Dotted lines mark boundaries of composite photos.

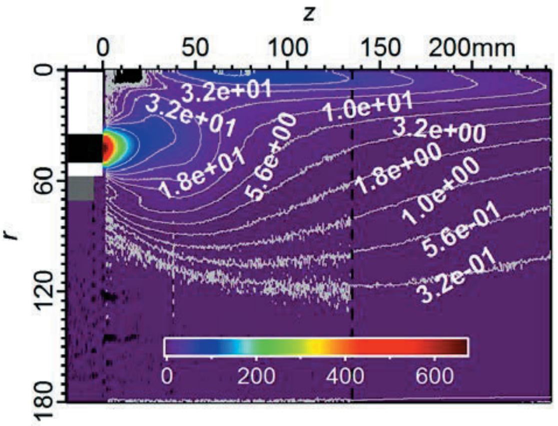

(a) Nominal Condition: Abel inversion of 542 nm radiance (arb. unit)

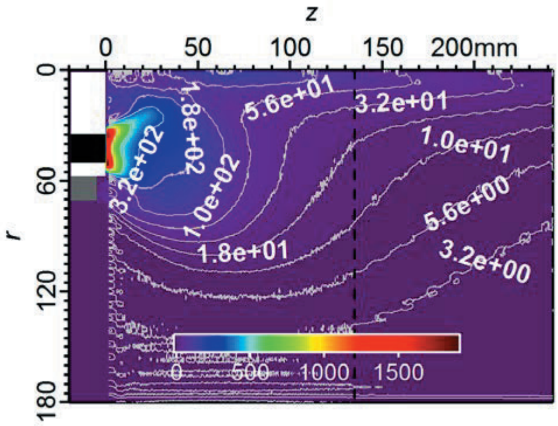

(b) Nominal Condition: Abel inversion of 823 nm radiance (arb. unit)

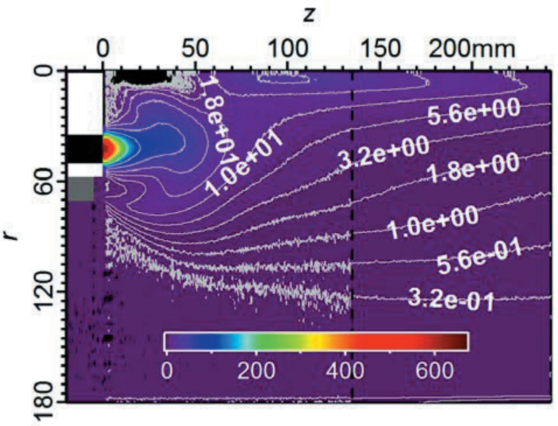

(c) Double Background Pressure Condition: Abel inversion of 542 nm radiance (arb. unit)

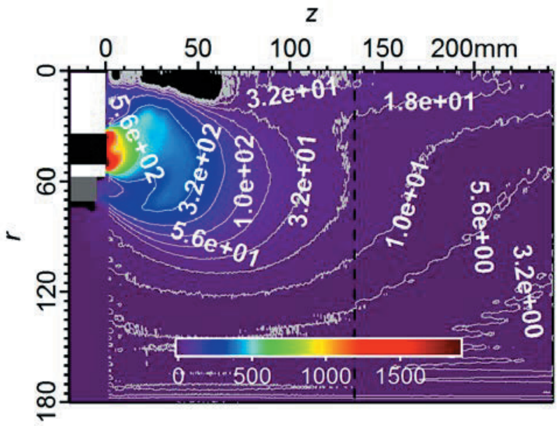

(d) Double Background Pressure Condition: Abel inversion of 823 nm radiance (arb. unit)

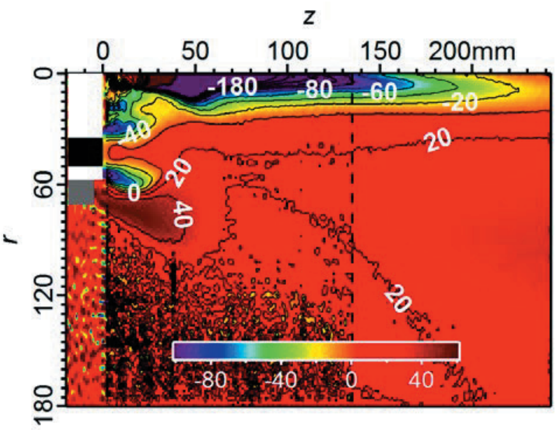

(e) Δ Abel Inv. R (%): $\frac{A_{R542:DP} - A_{R542:Nom}}{A_{R542:Nom}} \times 100$

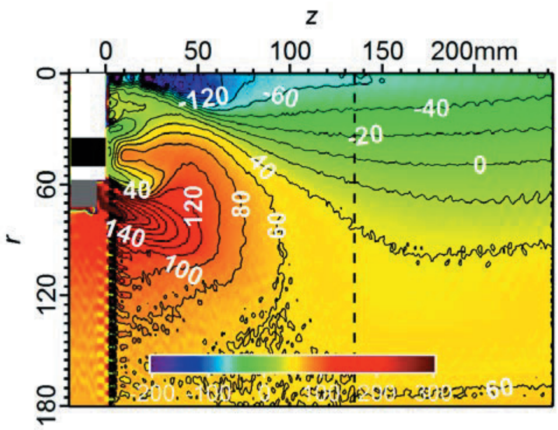

(f) Δ Abel Inv. R (%): $\frac{A_{R823:DP} - A_{R823:Nom}}{A_{R823:Nom}} \times 100$

Figure 8. Abel inversions of radiance of the nominal operating condition and the double background pressure condition. Black areas in plume represent negative values caused by asymmetry (central plume) or noise in cosine series fit (low intensity region). Dotted lines mark boundaries of composite photos.

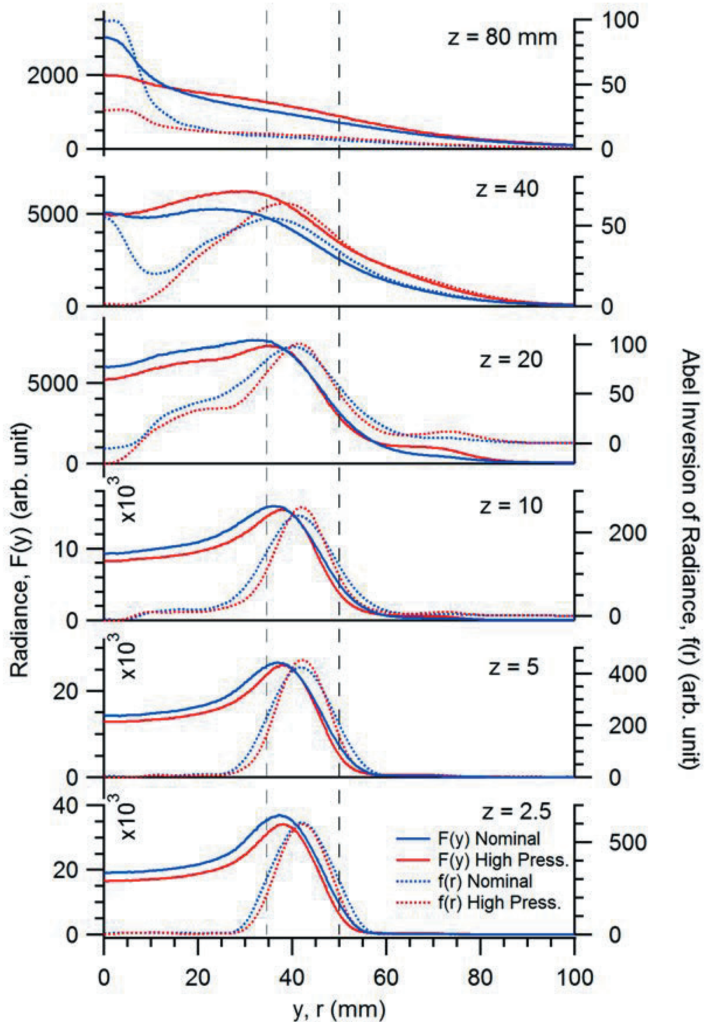

(a) 542 nm emission

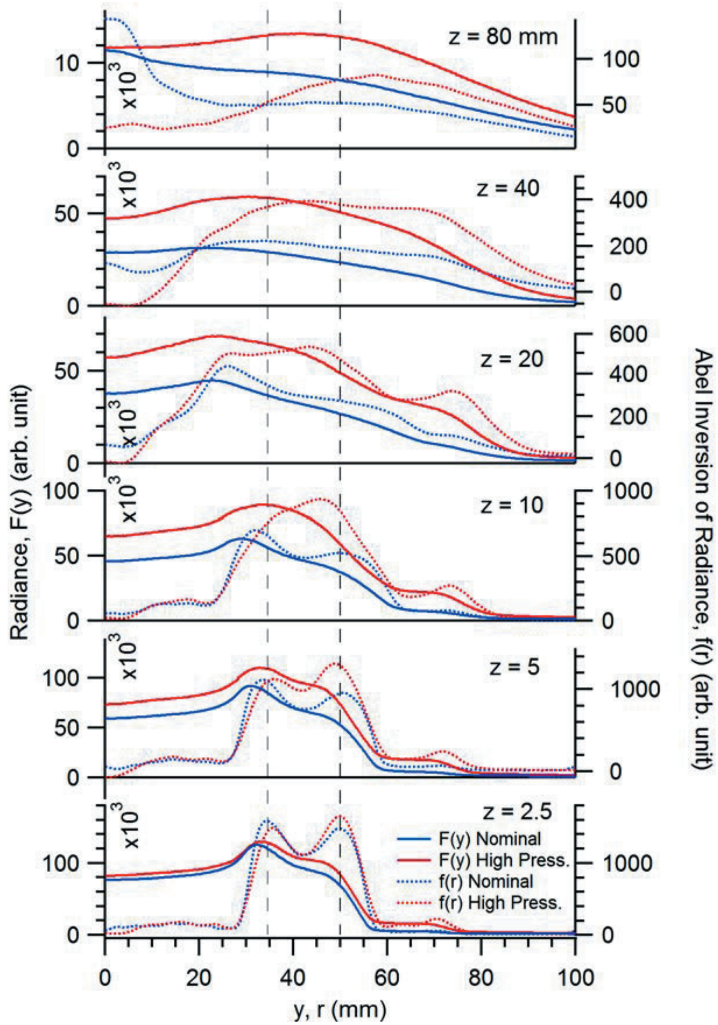

(b) 823 nm emission

Figure 9. Cross sections of radiance data for the nominal and high background pressure case at various z locations and their inverse Abel transforms. Dashed lines represent acceleration channel boundaries. Negative regions of Abel inversions are caused by plume asymmetry.

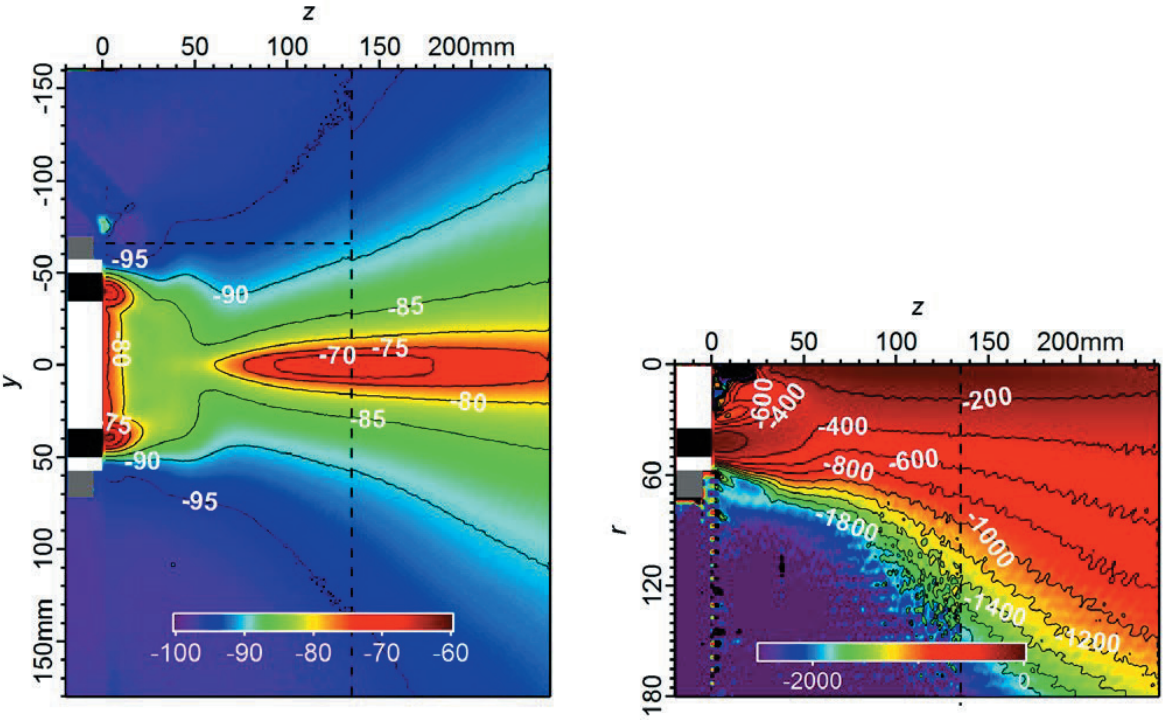

(a) Δ Radiance (%): $\frac{R_{542:Nom} - R_{823:Nom}}{R_{823:Nom}} \times 100$

(b) Δ Abel Inv. R (%): $\frac{A_{R542:Nom} - A_{R823:Nom}}{A_{R823:Nom}} \times 100$

Figure 10. Difference between 542 nm and 823 nm emission for nominal condition.

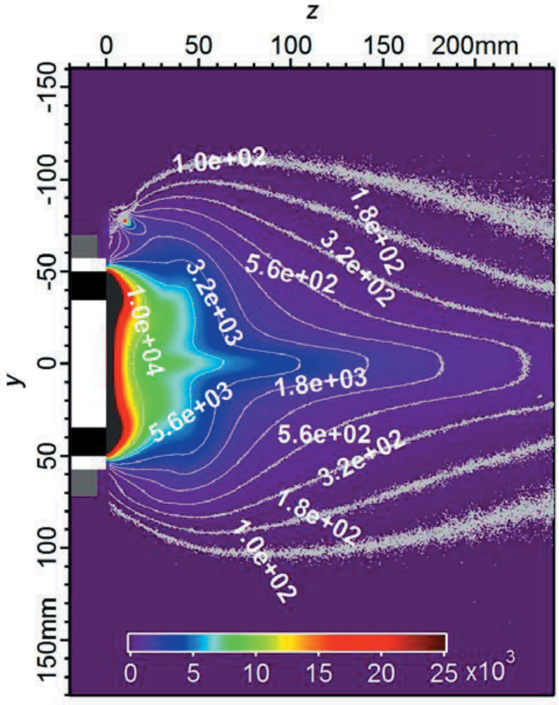

(a) V_d =210 V: 542 nm Radiance (arb. unit)

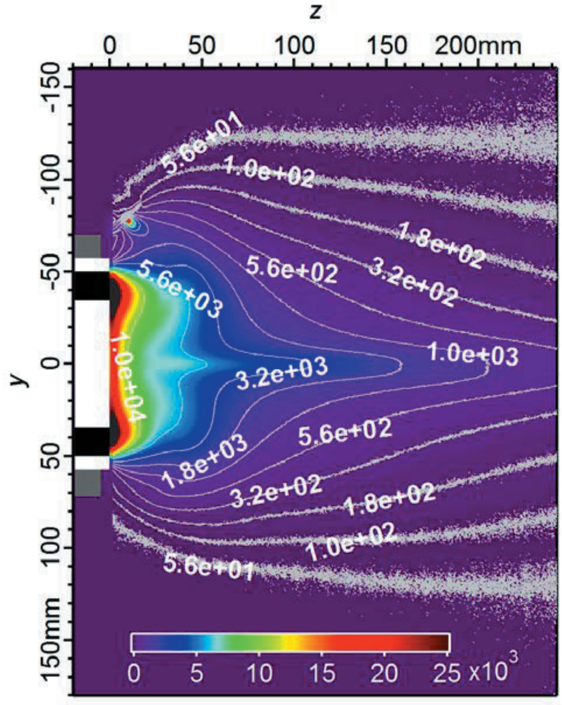

(b) V_d =390 V: 542 nm Radiance (arb. unit)

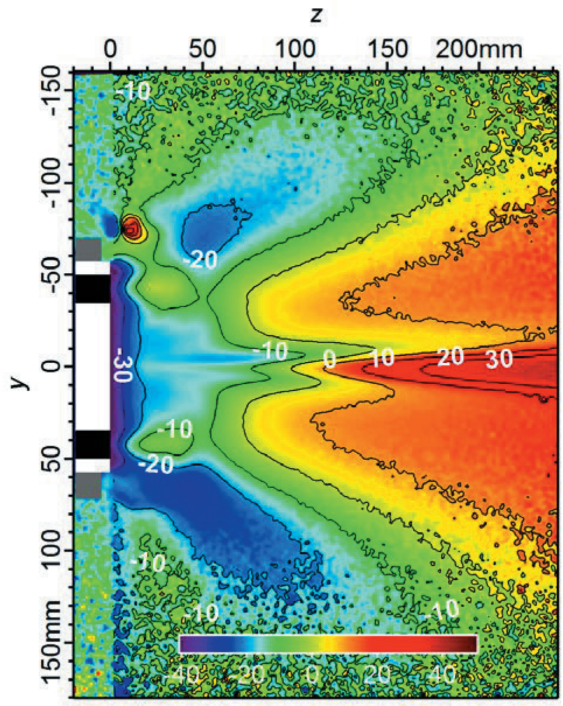

(c) Δ Radiance (%): $\frac{R_{542:Vd390} - R_{542:Vd210}}{R_{542:Vd210}} \times 100$

Figure 11. Ion emission radiance (542 nm) of the $V_d = 210$ V operating condition and the $V_d = 390$ V condition. Dark gray color in plume represents values greater than the color scale upper limit.

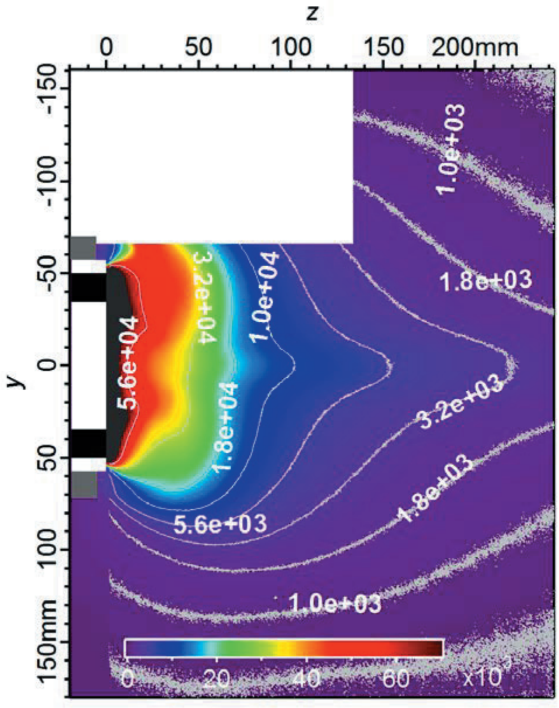

(a) V_d =210 V: 823 nm Radiance (arb. unit)

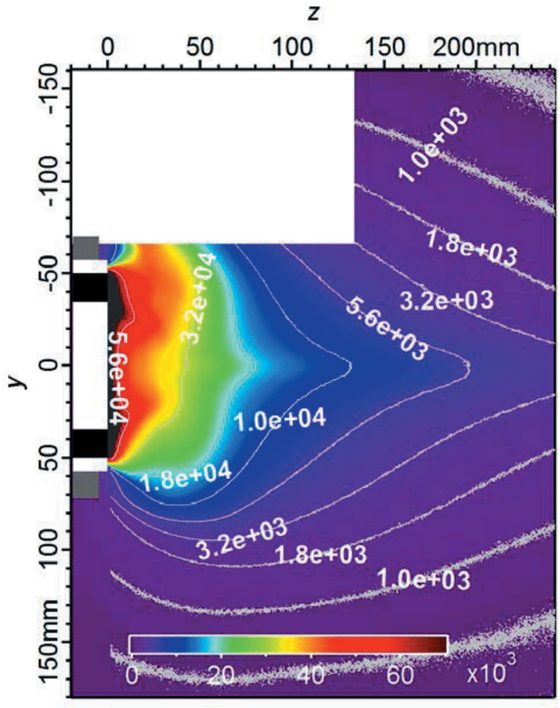

(b) V_d =390 V: 823 nm Radiance (arb. unit)

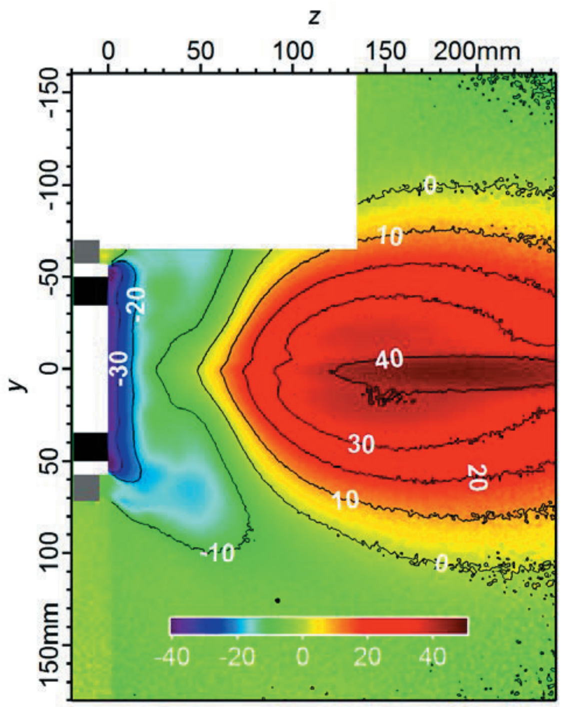

(c) Δ Radiance (%): $\frac{R_{823:Vd390} - R_{823:Vd210}}{R_{823:Vd210}} \times 100$

Figure 12. Neutral emission radiance (823 nm) of the V_d = 210 V operating condition and the V_d = 390 V condition. Dark gray color in plume represents values greater than the color scale upper limit. Missing image portion is where optical shade blocked view of cathode.

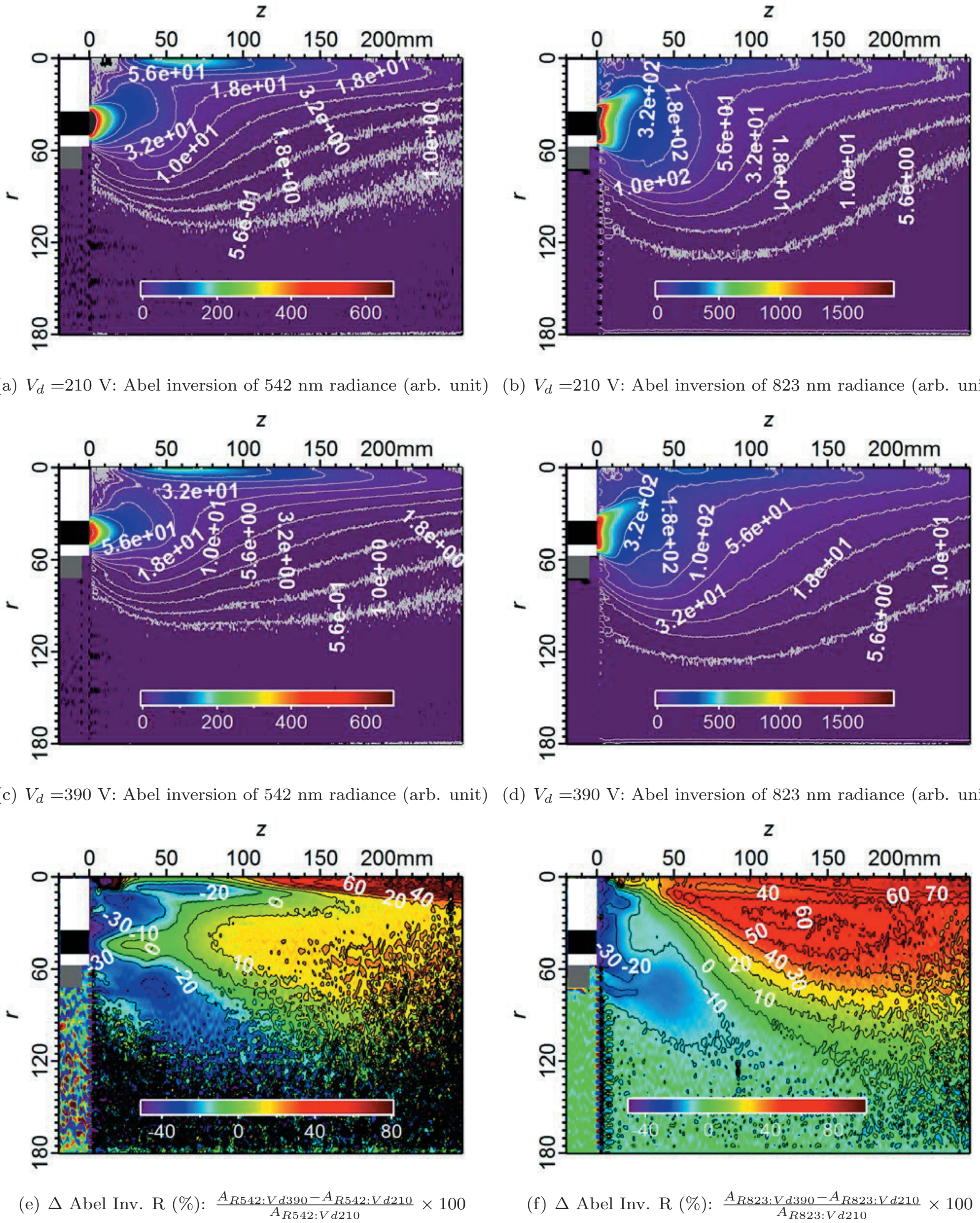

(a) V_d =210 V: Abel inversion of 542 nm radiance (arb. unit) (b) V_d =210 V: Abel inversion of 823 nm radiance (arb. unit)

(c) V_d =390 V: Abel inversion of 542 nm radiance (arb. unit) (d) V_d =390 V: Abel inversion of 823 nm radiance (arb. unit)

(e) Δ Abel Inv. R (%): $\frac{A_{R542:Vd390} - A_{R542:Vd210}}{A_{R542:Vd210}} \times 100$ (f) Δ Abel Inv. R (%): $\frac{A_{R823:Vd390} - A_{R823:Vd210}}{A_{R823:Vd210}} \times 100$

Figure 13. Abel inversions of radiance of the V_d = 210 V and V_d = 390 V operating conditions. Black areas in plume represent negative values caused by asymmetry (central plume) or noise in cosine series fit (low intensity region).

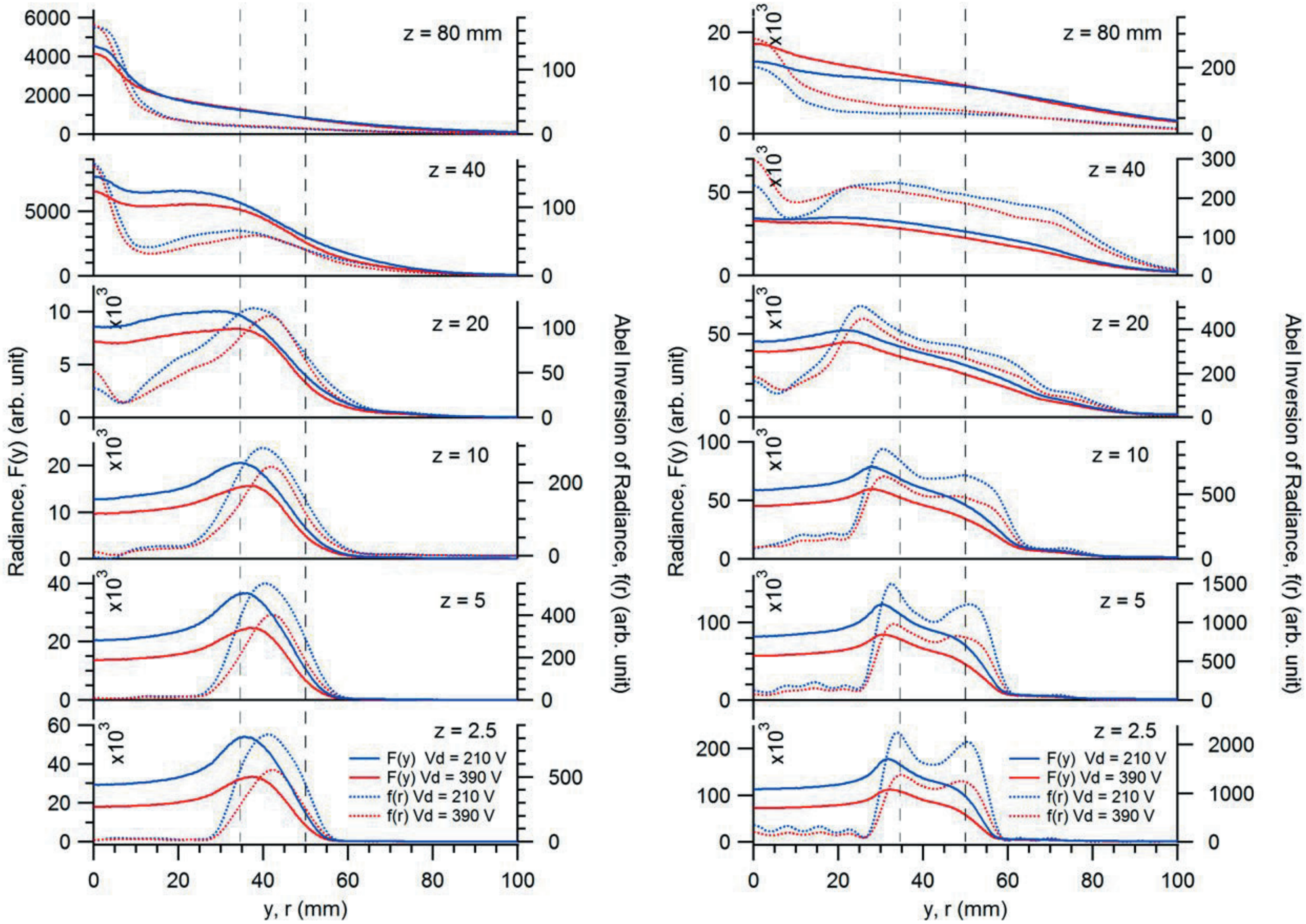

(a) 542 nm emission

(b) 823 nm emission

Figure 14. Cross sections of radiance data for the $V_d = 210$ V and $V_d = 390$ V cases at various z locations and their inverse Abel transforms. Dashed lines represent acceleration channel boundaries.

Conclusions

The imaging of a Hall thruster plume at different operating conditions with spectral line filters shows distinct changes in the emission structure from ions and neutral particles that reflect variations in plume density and temperature. Photographic measurements can be used as a convenient method for qualitatively examining plume structure, but may also provide a source of useful quantitative analysis when compared to collisional radiative models in numerical simulations or if they can be correlated to other diagnostic measurements of density and/or temperature.

The experimental techniques used in this study showed good results. Exposures of separate regions of the plume with various integration times and neutral density filters scaled remarkably well in magnitude and plume features blended almost seamlessly when combined for composite images. Overall, the Abel inversion of the photographic data appeared to resolve the evolution of the plume from the exit plane with good detail showing effects that corresponded with the channel geometry.

In the future, photographic measurements may be performed to match a numerically simulated data set that includes a collisional radiative model for model validation purposes. A more thorough optical calibration technique would allow absolute measurements of thruster radiance, which would add extra value for comparison. Performing Abel inversion analysis on a thruster with a centrally mounted cathode would likely produce even better results due to the high degree of plume symmetry. Near-field probe measurements of density may be performed to explore the possibility of using photographic data to estimate density values where temperature gradients are sufficiently low. It may be interesting to photograph these probes in the near-field plume to examine the effect their presence has on the plasma. The photographic techniques in this study may also be applicable to high-speed photography where time-resolved measurements could be used to study emission as a function of thruster breathing mode oscillations.

References

[1]Hargus Jr., W. A. and Cappelli, M. A., "Laser-Induced Fluorescence Measurements of Velocity within a Hall Discharge," *Applied Physics B*, Vol. 72, No. 8, June 2001, pp. 961–969.

[2]Reed, G. D., William A. Hargus, J., and Cappelli, M. A., "Microwave interferometry (90 GHz) for Hall Thruster Plume Density Characterization," *Proceedings of the 41st AIAA/ASME/SAE/ASEE Joint Propulsion Conference and Exhibit*, 2005, AIAA-2005-4399.

[3]Sekerak, M. J., *Plasma Oscillations and Operational Modes in Hall Effect Thrusters*, Ph.D. thesis, University of Michigan, 2014.

[4]Brown, D. L., *Investigation of Low Discharge Voltage Hall Thruster Characteristics and Evaluation of Loss Mechanisms*, Ph.D. thesis, University of Michigan, 2009.

[5]Sekerak, M. J. et al., "Azimuthal Spoke Propagation in Hall Effect Thrusters," *IEEE Transactions On Plasma Science*, Vol. 43, No. 1, 2014, pp. 72–85.

[6]Roche, S., Bechu, S., Prioul, M., Pagnon, D., Gascon, N., Bouchoule, A., Magne, L., Lasgorceix, P., and Touzeau, M., "Plasma characterisation of an ATON-Hall thruster - Channel and plume investigation," *Proceedings of the 36th AIAA/ASME/SAE/ASEE Joint Propulsion Conference and Exhibit*, 2000, AIAA-2000-3523.

[7]Garner, C. E., Brophy, J. R., Polk, J. E., and Pless, L. C., "Cyclic Endurance Test of a SPT-100 Stationary Plasma Thruster," *In the Proceeding of the 30th AIAA/SAE/ASME/ASEE Joint Propulsion Conference and Exhibit*, 1994, AIAA-94-2856.

[8]Hutchinson, I., *Principles of Plasma Diagnostics*, Cambridge University Press, New York, 1994.

[9]Dribinski, V., Ossadtchi, A., Mandelshtam, V. A., and Reisler, H., "Reconstruction of Abel-transformable images: The Gaussian basis-set expansion Abel transform method," *Review of Scientific Instruments*, Vol. 73, No. 7, 2002, pp. 2634–2642.

[10]Pretzier, G., Jger, H., Neger, T., Philipp, H., and Woisetschlger, J., "Comparison of Different Methods of Abel Inversion Using Computer Simulated and Experimental Side-On Data," *Zeitschrift fr Naturforschung*, Vol. 47a, 1992, pp. 955–970.

[11]Fulge, H., Knapp, A., Eichhorn, C., Wernitz, R., Lohle, S., Fasoulaskand, S., and Herdrich, G., "Improved Abel Inversion Method for Analysis of Spectral and Photo-Optical Data of Magnetic Influenced Plasma Flows," *Proceedings of the 42nd AIAA Plasmadynamics and Lasers Conference*, 2011, AIAA-2011-3456.

[12]Matlock, T., Hargus, Jr., W., Larson, C., and Nakles, M., "Inversion Method for Reconstructing Hall Thruster Plume Parameters from Optical Measurements," *43rd AIAA/ASME/SAE/ASEE Joint Propulsion Conference*, Cincinnati, OH, 2007, AIAA-2007-5303.

[13]Diamant, K. D., Liang, R., and Corey, R. L., "The Effect of Background Pressure on SPT-100 Hall Thruster Performance," *Proceedings of the 50th AIAA/ASME/SAE/ASEE Joint Propulsion Conference*, 2014, AIAA-2014-3710.

[14]Nakles, M. R. and Hargus Jr., W. A., "Background Pressure Effects on Ion Velocity Distribution Within a Medium-Powered Hall Thruster," *Journal of Propulsion and Power*, Vol. 27, No. 4, 2011, pp. 737–743.

[15]Crofton, M. et al., "Neutral Density in the SPT-140 Near-Field Plume," *Proceedings of the 33rd International Electric Propulsion Conference*, 2013, IEPC-2013-399.

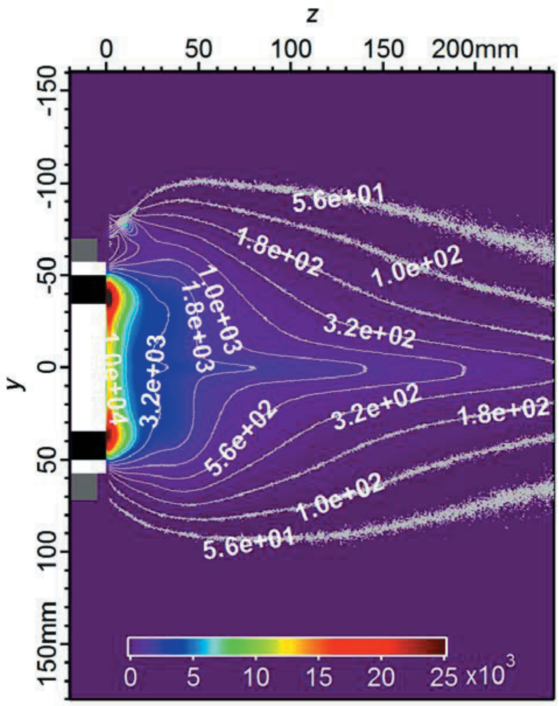

(a) $\dot{m}$ =-30%: 542 nm Radiance (arb. unit)

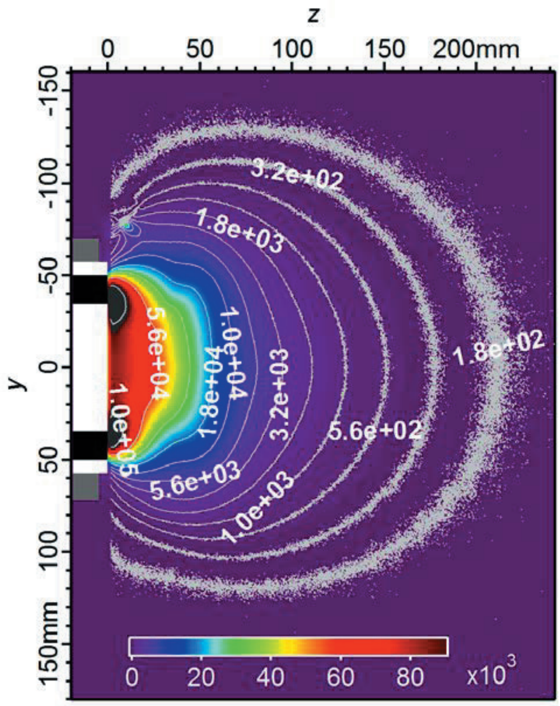

(b) $\dot{m}$ =+30%: 542 nm Radiance (arb. unit) Note: Color Scale Change

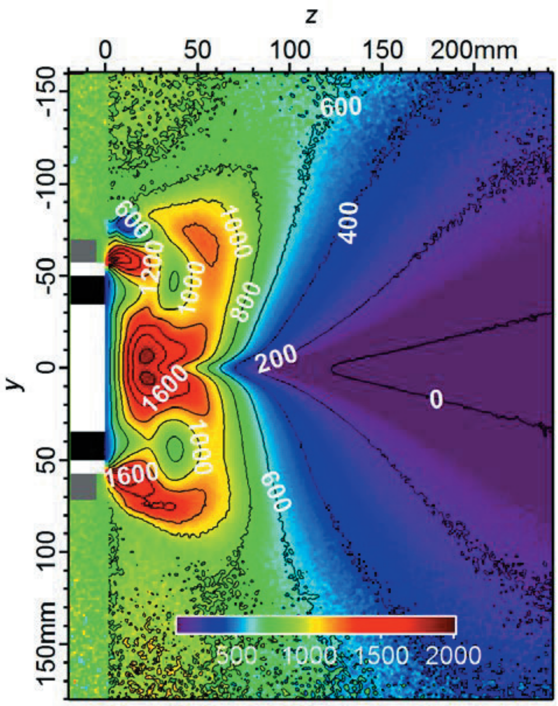

(c) Δ Radiance (%): $\frac{R_{542:m+30\%}-R_{542:m-30\%}}{R_{542:m-30\%}} \times 100$

Figure 15. Ion emission radiance (542 nm) of the $\dot{m}$ =-30% operating condition and the $\dot{m}$ =+30% condition. Dark gray color in plume represents values greater than the color scale upper limit.

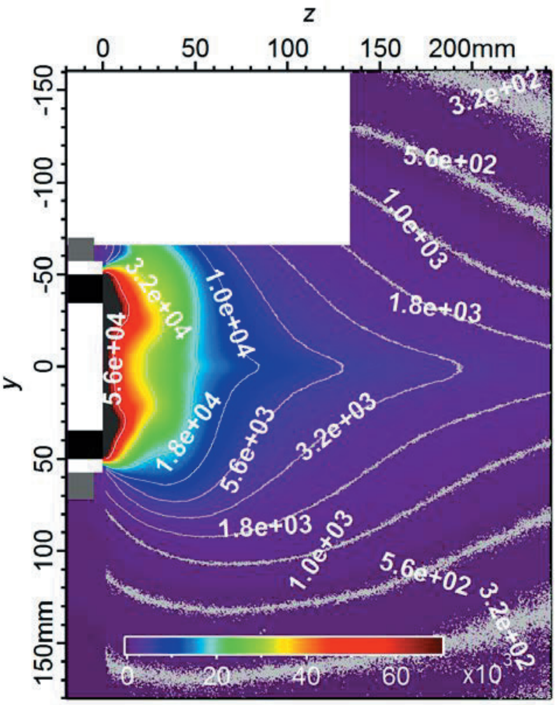

(a) $\dot{m}$ =-30%: 823 nm Radiance (arb. unit)

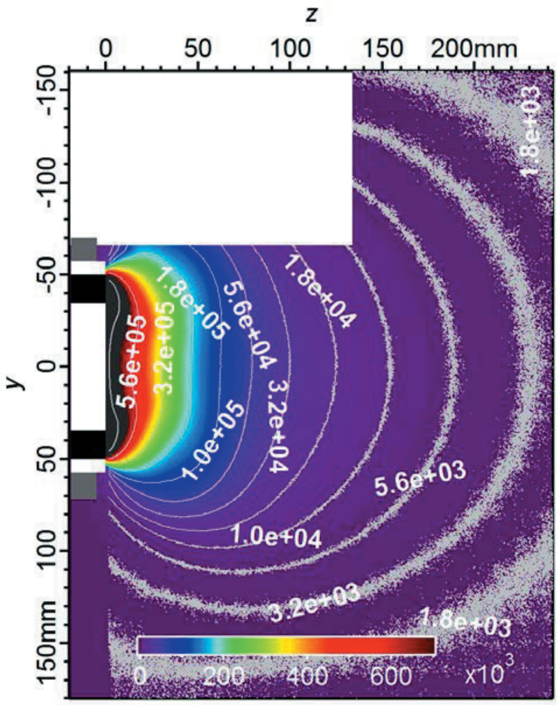

(b) $\dot{m}$ =+30%: 823 nm Radiance (arb. unit) Note: Color Scale Change

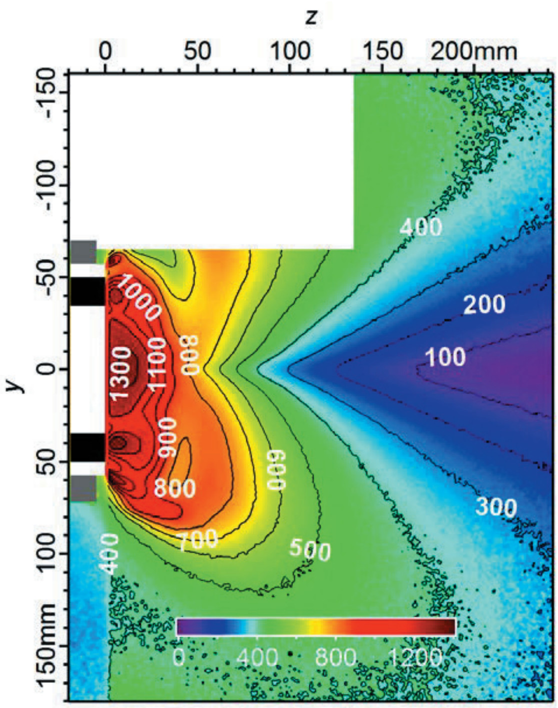

(c) Δ Radiance (%): $\frac{R_{823:m+30\%} - R_{823:m-30\%}}{R_{823:m-30\%}} \times 100$

Figure 16. Ion emission radiance (823 nm) of the $\dot{m}$ =-30% operating condition and the $\dot{m}$ =+30% condition. Dark gray color in plume represents values greater than the color scale upper limit. Missing image portion is where optical shade blocked view of cathode.

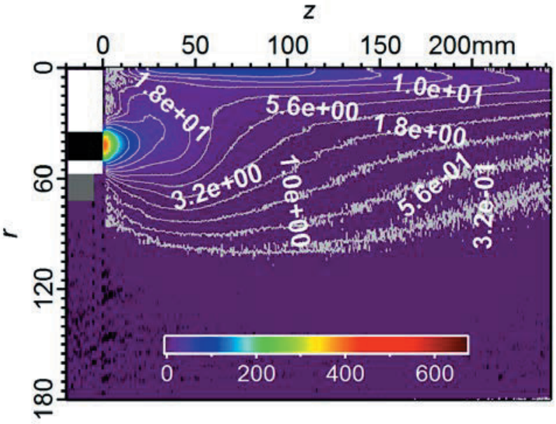

(a) $\dot{m}$ =-30%: Abel inversion of 542 nm radiance (arb. unit)

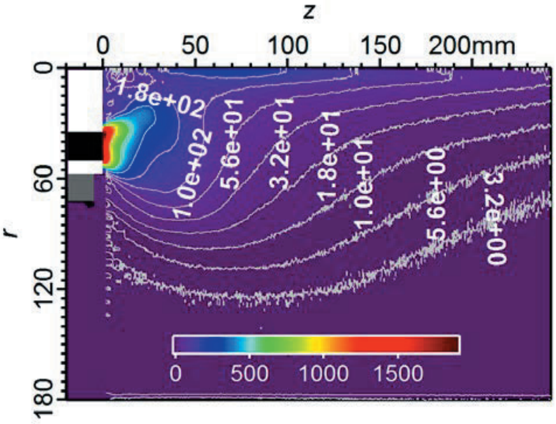

(b) $\dot{m}$ =-30%: Abel inversion of 823 nm radiance (arb. unit)

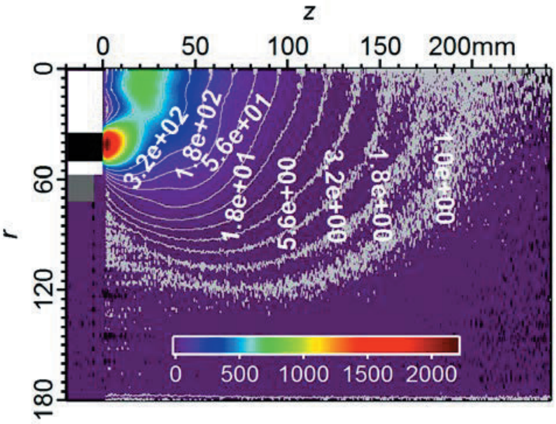

(c) $\dot{m}$ =+30%: Abel inversion of 542 nm radiance (arb. unit)

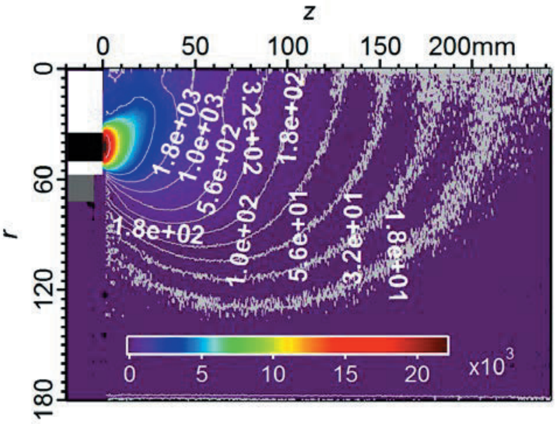

(d) $\dot{m}$ =+30%: Abel inversion of 823 nm radiance (arb. unit)

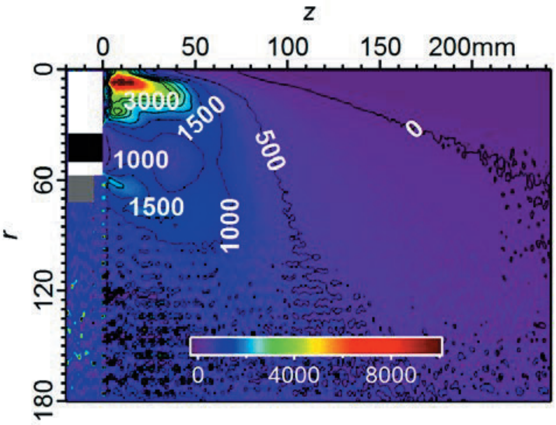

(e) Δ Abel Inv. R (%): $\frac{A_{R542:m+30\%} - A_{R542:m-30\%}}{A_{R542:m-30\%}} \times 100$

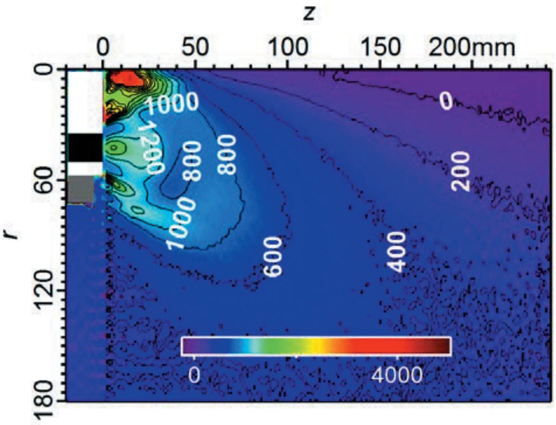

(f) Δ Abel Inv. R (%): $\frac{A_{R823:m+30\%} - A_{R823:m-30\%}}{A_{R823:m-30\%}} \times 100$

Figure 17. Abel inversions of radiance of the $\dot{m}$ =-30% and $\dot{m}$ =-30% operating conditions. Black areas in plume represent negative values caused by asymmetry (central plume) or noise in cosine series fit (low intensity region).